

Electronic Supplementary Information

Photo-Irradiation Tunes Highly Active Sites over β -Ni(OH)₂ Nanosheets for Electrocatalytic Oxygen Evolution Reaction

Chengan Liao,^{a,‡} Ziyi Xiao,^{a,‡} Ning Zhang,^{*a,b} Bo Liang,^a Gen Chen,^a Wei Wu,^b Jianglin Pan,^c Min Liu,^c Xiang-Rong Zheng,^d Qing Kang,^e Xianwu Cao,^b Xiaohe Liu,^{a,f} Renzhi Ma^g

^a School of Materials Science and Engineering, Central South University, Changsha 410083, Hunan, P. R. China

Email: nzhang@csu.edu.cn

^b Guangdong Provincial Key Laboratory of Technique and Equipment for Macromolecular Advanced Manufacturing, South China University of Technology, Guangzhou 510640, Guangdong, P. R. China

^c School of Physical Science and Electronics Central South University, Changsha, Hunan 410083, P. R. China

^d Department of Pediatrics, Xiangya Hospital, Central South University, 87 Xiangya Road, Changsha 410008, Hunan, P. R. China

^e Institute of Surface Analysis and Chemical Biology, University of Jinan, Jinan, Shandong 250022, P. R. China

^f School of Chemical Engineering and Energy, Zhengzhou University, Zhengzhou 450001, P. R. China

^g International Center for Materials Nanoarchitectonics (MANA), National Institute for Materials Science (NIMS), 1-1 Namiki, Tsukuba, Ibaraki 305-0044, Japan

[‡] These authors contribute equally to this work.

Experimental Section

Characterization

X-ray diffraction profiles were recorded by a RIGAKU Rint-2000 X-ray diffractometer equipped with graphite monochromatized Cu-K α radiation ($\lambda=1.54184$ Å). TEM images were recorded by FEI Tecnai G2 F20 field emission transmission electron microscopy operated at 200 kV. SEM images were recorded by TESCAN MIRA field emission scanning electron microscopy. The X-ray photoelectron spectroscopy spectra was performed using a Thermo Fisher ESCALAB 250Xi spectrophotometer (the C 1s at 284.8 eV from adventitious carbon is used to calibrate the XPS spectrum). Nitrogen adsorption-desorption isotherms were performed on a Quadrachrome adsorption instrument (Autosorb-iQ3; Quantachrome, America) at 77 K. Brunauer-Emmett-Teller (BET) method and the Barrett-Joyner-Halenda (BJH) model were employed to calculate the specific surface area and pore size distribution. The EPR spectra were performed using a Bruker A300 electron paramagnetic resonance spectrometer. The X-ray absorption spectroscopy experiments were performed at the National Synchrotron Radiation Research Center (NSRRC) in Taiwan. In-situ Raman characteristics were performed using a spectroelectrochemical cell (ECC-Opto-Std-Aqu, EL-Cell GmbH, Hamburg, Germany) that uses an Ag/AgCl reference electrode. The potentials measured were converted to RHE.

Preparation of β -Ni(OH) $_2$ Nanosheets

The β -Ni(OH) $_2$ nanosheets were synthesized by hydrothermal method. Approximate 20mL of 0.1 M NaOH and 20mL of 0.05 M NiCl $_2$ solution were mixed under

vigorous magnetic stirring. Then, the green solution was transferred into a 50 mL Teflon-lined stainless-steel autoclave and kept in oven at 100 °C for 12 h. The obtained products were collected and washed with deionized water and ethanol for several times. Finally, the green powder was obtained by drying at 60 °C for 10 h.

Preparation of Light-irradiated β -Ni(OH)₂ Nanosheets

In a typical process, 200 mg β -Ni(OH)₂ nanosheets were dispersed in 200 mL deionized water under magnetic stirring. After β -Ni(OH)₂ dissolved completely, the solution was irradiated by a 300W Xe lamp for 10-30 h. Finally, the obtained products were washed with deionized water and ethanol for several times, which were drying at 60 °C for about 10 h. These products were marked as β -Ni(OH)₂-10h, β -Ni(OH)₂-20h, and β -Ni(OH)₂-30h. The α -Ni(OH)₂ nanosheets were prepared through an alcohothermal method. Typically, 0.4 g of NiCl₂·6H₂O was added in 40 mL ethanol. The mixture was stirred until a transparent solution was observed. Then, the solution was transferred into 50 mL Teflon-lined stainless-steel autoclave and kept in oven at 150 °C for 12 h. The obtained products were collected and washed by ethanol for several times. Finally, the green powder was obtained by drying at 60 °C for 10 h.

Three-electrodes electrochemical measurement

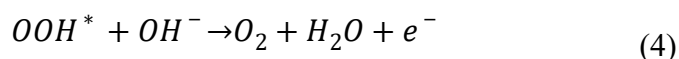
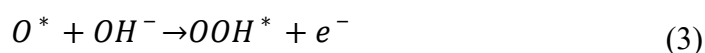
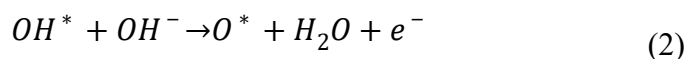
Electrochemical experiments were measured on a CHI 760E electrochemical workstation in a three-electrode cell and gas flow control systems at room temperature. A Hg/HgO (1 M KOH) electrode and a carbon rod was used as reference electrode and counter electrode. The rotating ring disk electrode (RRDE) modified with catalyst was used as the working electrode. The catalyst ink was prepared by dispersing a 10

mg catalyst in 1 mL ethanol and 1mL deionized water to form ethanol/water solution. Subsequently, 15 μ L Nafion solution (Nafion D-521 5% w/w in water and 1-propano, Alfa Aesar Co. Ltd.) was added to the ink as a proton conducting binder. To form a homogeneous solution, the catalyst ink was ultrasonic dispersed for 30 min and vigorously stirred for 12h at room temperature. After polishing the electrode with a suspension of alumina, the surface of RRDE was coated with 4 μ L of the catalyst ink. The catalyst loading was about 0.285mg cm^{-2} . The pasted catalyst on the working electrode was dried at 60 $^{\circ}\text{C}$ in vacuum for further use. All OER measurements were carried out in 1M KOH solution which was purged with high-purity nitrogen for 15 min. All polarization curves were corrected with 95% iR compensation. After cycling the working electrode potential between 0.9 V and 1.7 V at 30 mV s^{-1} for 30 cycles, the polarization curves were recorded from 0.9 V to 1.7 V at 10 mV s^{-1} with a rotation rate of 1600 rpm. The current density was normalized to the geometrical surface area and the potentials (vs. Hg/HgO) were corrected to the reversible hydrogen electrode (RHE) according to the equation: $E_{\text{RHE}} = E_{\text{Hg/HgO}} + 0.059 \times \text{pH} + 0.098$. Tafel slopes were obtained from the corresponding LSV curves according to the equation: $\eta = a + b \cdot \log j$ (η is the overpotential, j is the anodic current density, and b is the Tafel slope). The electrochemical impedance spectroscopy (EIS) was measured at 1.55 V (vs. RHE) in the frequency range from 10^5 to 0.1 Hz with an amplitude of 5 mV. The cycling stability curve was collected by a chronopotentiometry response in N_2 -saturated 1 M KOH solution at the current density of 10 mA cm^{-2} for several hours.

DFT Calculation

To further understand the effect of exposed crystal facets on OER, first-principles calculations were carried out by using Vienna Ab initio Simulation Package (VASP). Projector augmented wave (PAW) was adopted to describe electron interactions. The Perdew–Burke–Ernzerhof (PBE) functional of the generalized gradient approximation (GGA) was used as the exchange–correlation function. To optimization of (001), (100), and (011) surface, all the model was constructed with a 20 Å vacuum layer region in the z direction to minimize the interactions between adjacent image cells by relaxed via the conjugate-gradient method. To confirm the strong correlated electronic states of Ni, a GGA+U method was used. In this study, we used Hubbard U of 3.8 eV for the calculation of Ni d-states. During all calculations, the energies change criterion was set to 10^{-4} eV, and the atoms were relaxed until the force acting on each atom was less than 0.01 eV Å⁻¹. The plane-wave basis set was within the kinetic cutoff energy of 500 eV for all compute instances. The adsorption energy of intermediates on the surface of (001), (100), and (011) face were calculated using the following method:

In alkaline conditions, the OER process currently involve four elementary reaction steps:



Where * and X* represent an active site and an adsorbed X intermediate (X=OH, O, and OOH) on the surface, respectively. Based on the above OER steps, the relevant

computational models of intermediates adsorbed on the surface of (001), (011) and (100) facets for β -Ni(OH)₂ were constructed; the detailed models are presented in **Fig. S9**.

Adsorption energy of intermediates (O^* , OH^* , OOH^*) on ($*$) substrate were determined by the following approach of Nøeskov et al.

$$\Delta E_{OH^*} = E(OH^*) - E(*) - \left(E_{H_2O} - \frac{1}{2} E_{H_2} \right) \quad (5)$$

$$\Delta E_{O^*} = E(O^*) - E(*) - (E_{H_2O} - E_{H_2}) \quad (6)$$

$$\Delta E_{OOH^*} = E(OOH^*) - E(*) - (2E_{H_2O} - 3/2 E_{H_2}) \quad (7)$$

Where $E(*)$, $E(HO^*)$, $E(O^*)$, and $E(HOO^*)$ are the total energies of the pure surface and the adsorbed surface with HO^* , O^* , and HOO^* , respectively, which can be got from the calculations. E_{H_2O} and E_{H_2} are the computed energies for the sole H₂O and H₂ molecules, respectively.

The Gibbs free energy changes of intermediates adsorbed on the surface of catalysts were calculated with zero point energy and entropy corrections using the following computational formula:

$$\Delta G_{X^*} = \Delta E_{X^*} + (\Delta ZPE - T\Delta S)_{X^*} \quad (8)$$

Where ZPE , T , and S are the zero point energy, temperature, and entropy, respectively.

The Gibbs free energy changes for steps 1-4 can be expressed as follows:

$$\Delta G_1 = \Delta G_{OH^*} - eU \quad (9)$$

$$\Delta G_2 = \Delta G_{O^*} - \Delta G_{OH^*} - eU \quad (10)$$

$$\Delta G_3 = \Delta G_{OOH^*} - \Delta G_{O^*} - eU \quad (11)$$

$$\Delta G_4 = 4.92[eV] - \Delta G_{OOH^*} - eU \quad (12)$$

Where U is the applied voltage, in this study, $U=0$, and the total free energy (ΔG) to form one molecule of O_2 was fixed at the value of 4.92 eV in order to avoid the calculation of the O_2 bond energy, which is difficult to determine accurately within GGA-DFT.

Additional Figures and Tables

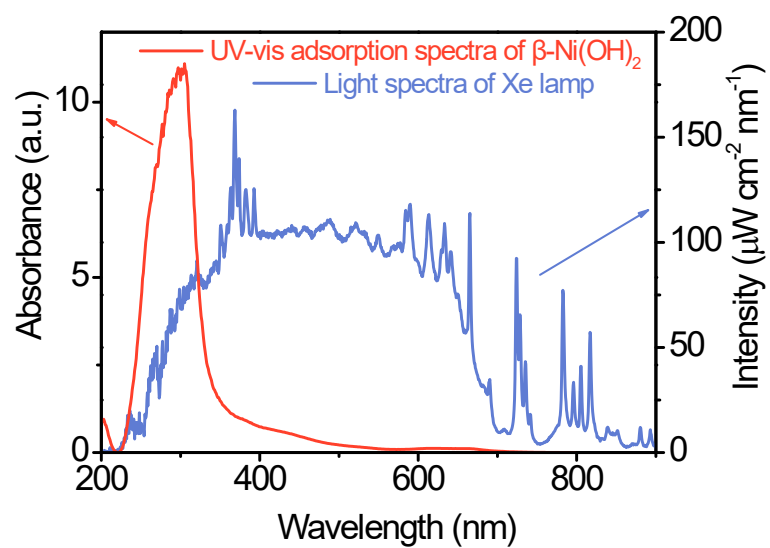


Fig. S1 UV-vis adsorption spectra of $\beta\text{-Ni(OH)}_2$ and light spectrum of used Xe lamp.

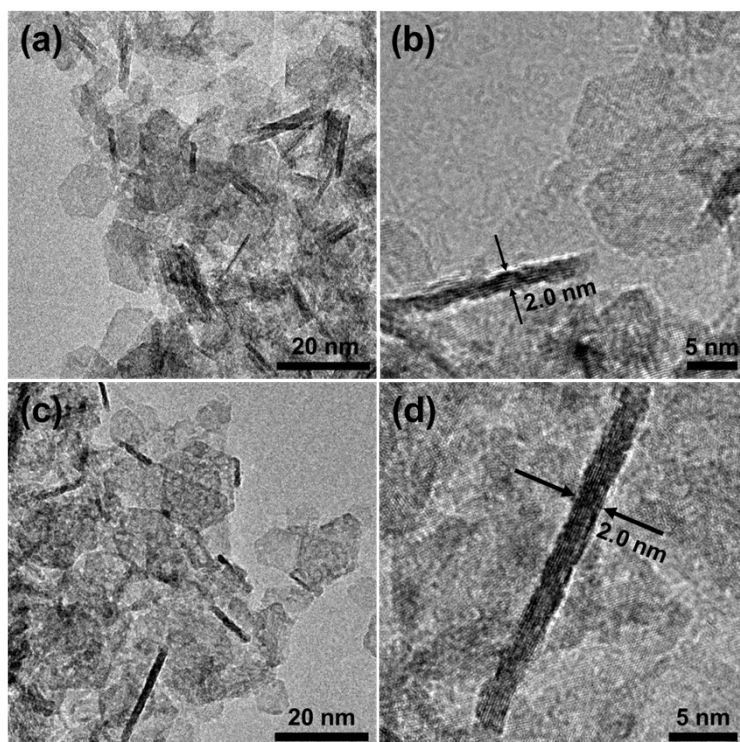


Fig. S2 (a, b) The TEM images of pristine β -Ni(OH)₂ nanosheets; (c, d) The TEM images of β -Ni(OH)₂-30h nanosheets.

Fig. S2a shows the typical TEM image of pristine β -Ni(OH)₂, displaying that the product is in the form of thin nanosheet. The size of these nanosheets is approximate 10 nm. TEM image in **Fig. S2b** shows that a vertically positioned β -Ni(OH)₂ nanosheet with thickness about 2.0 nm. For β -Ni(OH)₂ nanosheets with Xe lamp irradiating for 30 h (β -Ni(OH)₂-30h), there is no obviously changes in size and thickness (**Fig S2c and d**).

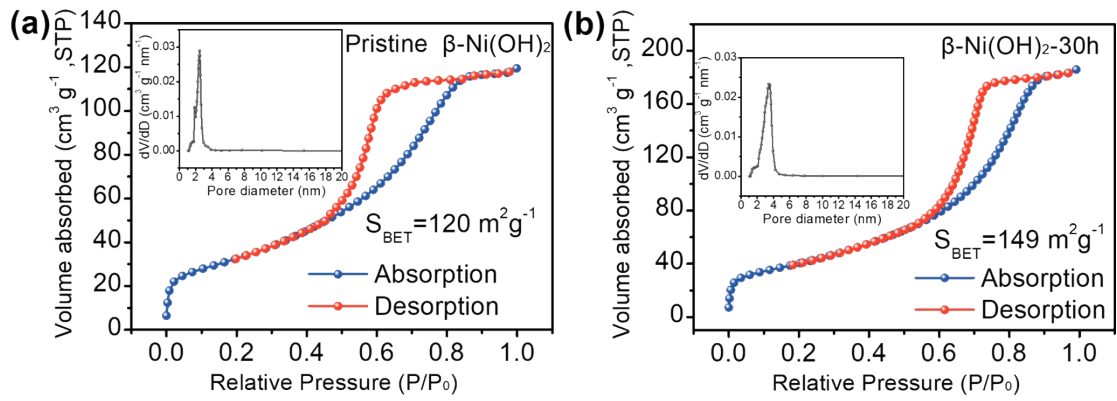


Fig. S3 N₂ adsorption and desorption of (a) pristine β-Ni(OH)₂ and (b) β-Ni(OH)₂-30h.

The specific surface areas of these catalysts were analyzed by N₂ absorption-desorption, as shown in Fig. S3. The Brunauer-Emmett-Teller (BET) surface area of the pristine β-Ni(OH)₂ nanosheets is calculated to be 120 m² g⁻¹. For the β-Ni(OH)₂-30 h nanosheets, the BET surface area is calculated to be 149 m² g⁻¹. The BET surface area of β-Ni(OH)₂-30 h nanosheets is slightly increased compared to that of the pristine β-Ni(OH)₂ nanosheets, which is probably caused by the produced defects and pores.

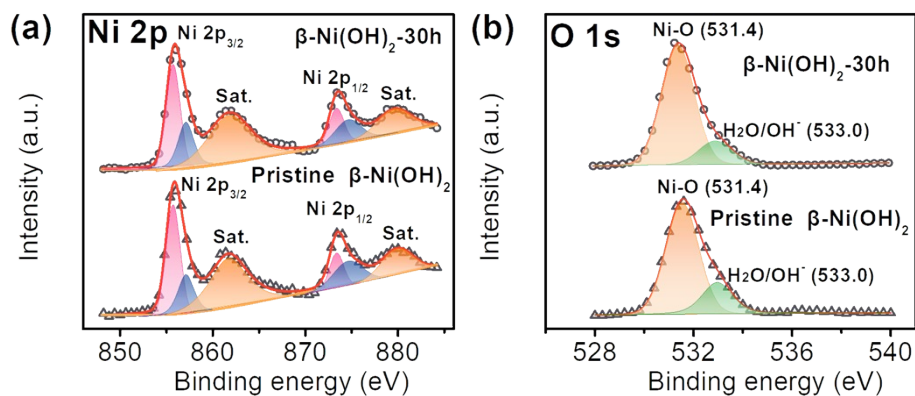


Fig. S4 (a) Ni 2p and (b) O 1s XPS spectra of pristine $\beta\text{-Ni(OH)}_2$ and $\beta\text{-Ni(OH)}_2\text{-30h}$.

The XPS spectra of Ni 2p in Fig. S4a show two major peaks centered around 855.9 and 873.6 eV, corresponding to Ni 2p_{3/2} and Ni 2p_{1/2}, respectively.^{1, 2} In addition, the shake-up satellite peaks located at 861.9 and 879.7 eV appears in both light-irradiated and pristine nanosheets. The spin-energy separation of Ni 2p_{1/2} and Ni 2p_{3/2} is about 17.7 eV, which is the characteristic of Ni(OH)₂.² In Fig. S4b, the O 1s spectra of two products are divided into two peaks at 531.4 and 533.0 eV, which is ascribed to Ni-O and -OH.¹ There is no obvious changes in XPS spectra between pristine $\beta\text{-Ni(OH)}_2$ and $\beta\text{-Ni(OH)}_2\text{-30}$, suggesting that the chemical states of Ni and O in both are identical.

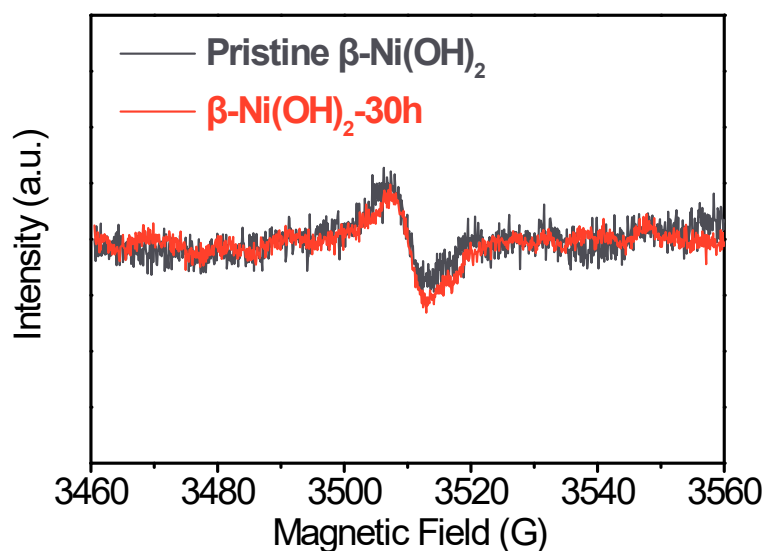


Fig. S5 EPR spectra of pristine $\beta\text{-Ni(OH)}_2$ and $\beta\text{-Ni(OH)}_2\text{-30h}$.

In **Fig. S5**, The EPR signal at $g=2.003$ could be identified as the electrons trapped on oxygen vacancies and the intensity of peak indicates the concentration of oxygen vacancy.³ The signal intensity of oxygen vacancy on pristine $\beta\text{-Ni(OH)}_2$ is closed to that on $\beta\text{-Ni(OH)}_2\text{-30h}$, suggesting that the vacancy defects and vacancy concentrations are identical. Therefore, there is no obvious vacancy defects produced after the treatment of photo irradiation.

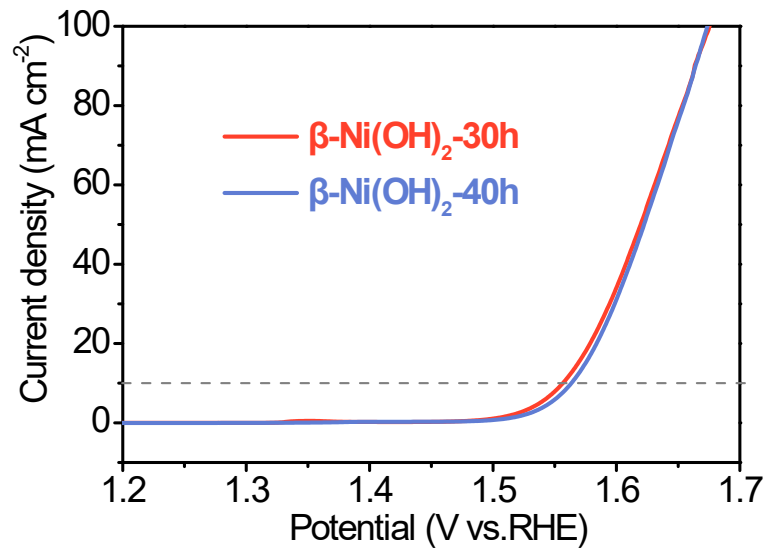


Fig. S6 LSV curves of $\beta\text{-Ni(OH)}_2\text{-30h}$ and $\beta\text{-Ni(OH)}_2\text{-40h}$.

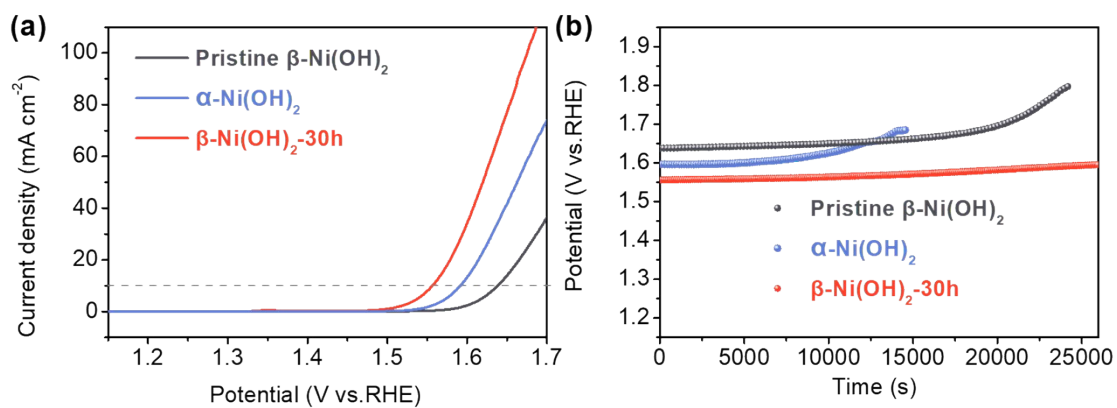


Fig. S7 (a) OER performance of the pristine β -Ni(OH) $_2$, α -Ni(OH) $_2$, and β -Ni(OH) $_2$ -30h in 1M KOH; (b) chronopotentiometry curves of pristine β -Ni(OH) $_2$, α -Ni(OH) $_2$, and β -Ni(OH) $_2$ -30h under a constant current density of 10 mA cm $^{-2}$.

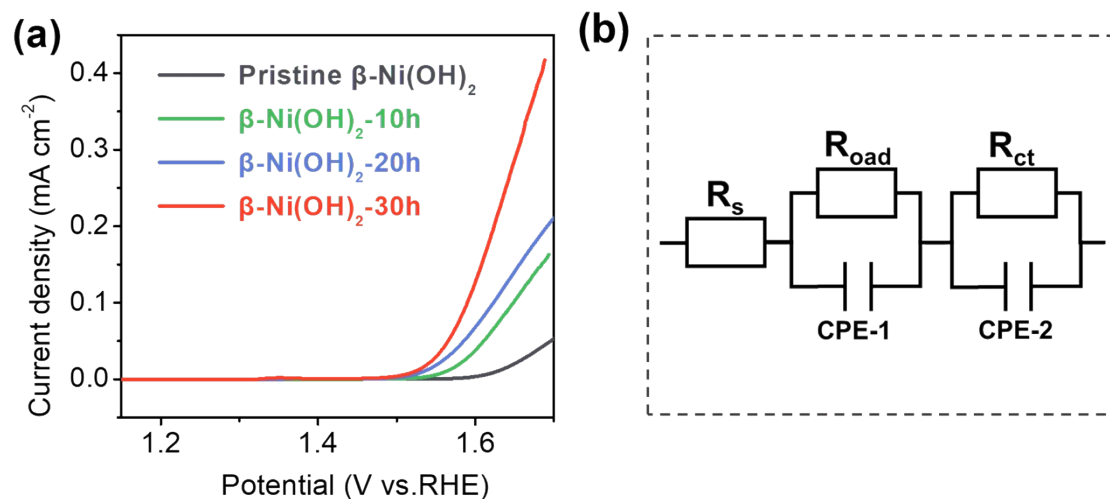


Fig. S8 (a) LSV curves normalized with ECSA for pristine $\beta\text{-Ni(OH)}_2$ and photo irradiated $\beta\text{-Ni(OH)}_2$; (b) The equivalent circuit model used to fit resistance.

In simulated circuit, R_s is electrolyte resistance, R_{ct} corresponds to charge transfer resistance, and R_{oad} stands for the resistance of surface intermediates adsorptions. A constant phase element (CPE) is applied to obtain reasonable fittings, which means that the process of charge transfer and polarization are deviated from an ideal capacitor behavior.

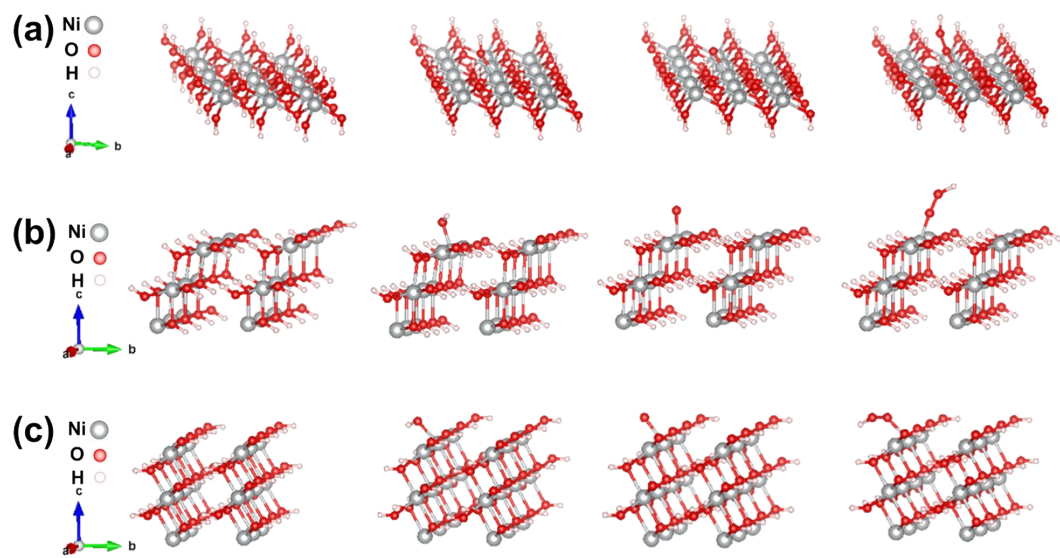


Fig. S9 The optimized atomic models for intermediates adsorptions on (a) (001) , (b) (011) and (c) (100) facets of β -Ni(OH)₂.

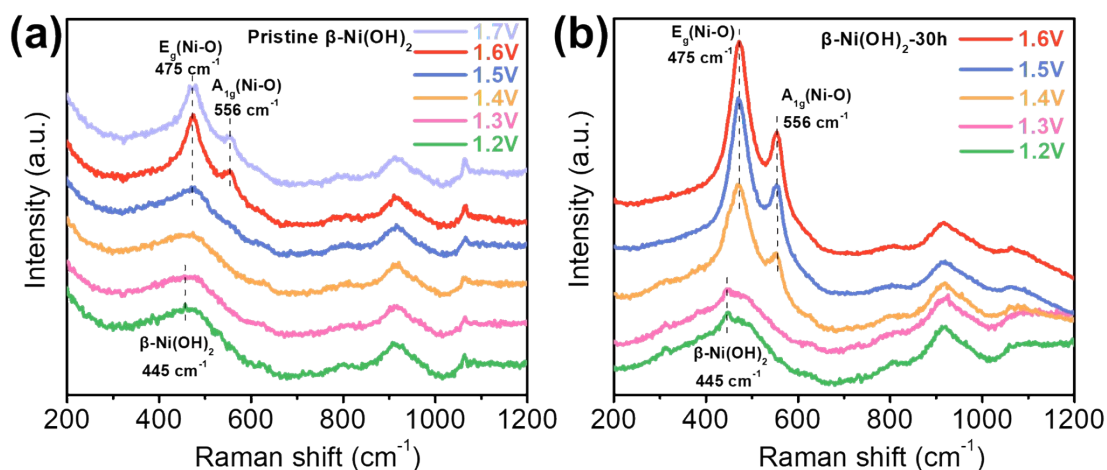


Fig. S10 In situ Raman spectra of (a) pristine $\beta\text{-Ni(OH)}_2$ and (b) $\beta\text{-Ni(OH)}_2\text{-30h}$ at different potentials.

In situ Raman spectroscopy was employed to investigate the structural changes during the OER process. Fig. S10a shows the Raman spectrum of pristine $\beta\text{-Ni(OH)}_2$ at different applied potentials. The Ni–O peak located at 445 cm^{-1} is ascribed to the $\beta\text{-Ni(OH)}_2$ phase, which is maintained at low potentials from 1.2 to 1.5 V.⁴ When the potential increases to 1.6 V, $\beta\text{-Ni(OH)}_2$ transforms to NiOOH, as observed from the emergence of two Raman peaks located at 475 and 576 cm^{-1} , which are ascribed to the E_g Ni-O bending and A_{1g} Ni-O stretching vibration modes, respectively.^{5, 6} As shown in Fig. S10b, the structural transformation of $\beta\text{-Ni(OH)}_2\text{-30 h}$ occurs at 1.4 V, indicating that the destroyed surface of $\beta\text{-Ni(OH)}_2\text{-30 h}$ is more easily oxidized to NiOOH. In addition, the intensity ratio of the I_{475} and I_{556} peaks in $\beta\text{-Ni(OH)}_2\text{-30 h}$ is much higher than that in pristine $\beta\text{-Ni(OH)}_2$. A higher ratio of I_{475} and I_{556} is usually associated with more of the NiOOH phase, which serves as the active species of most Ni-based catalysts for OER.⁷

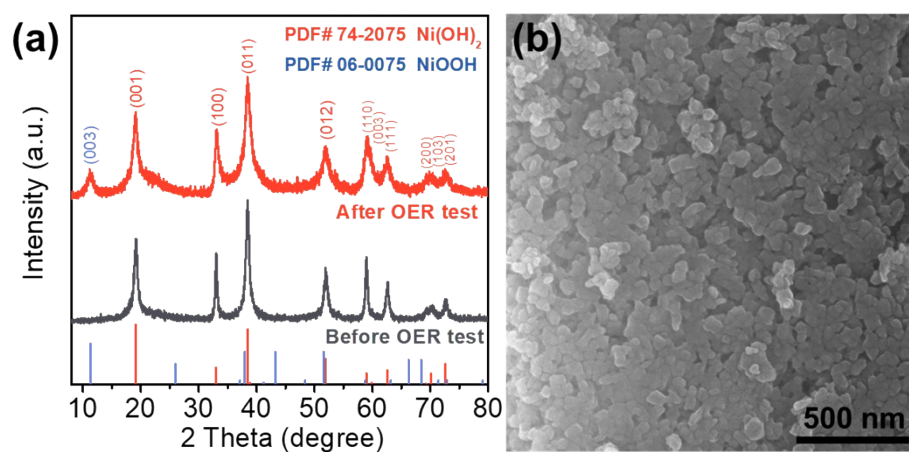


Fig. S11 (a) XRD patterns of β -Ni(OH)₂-30h before and after OER test; (b) SEM image of β -Ni(OH)₂-30h after OER test.

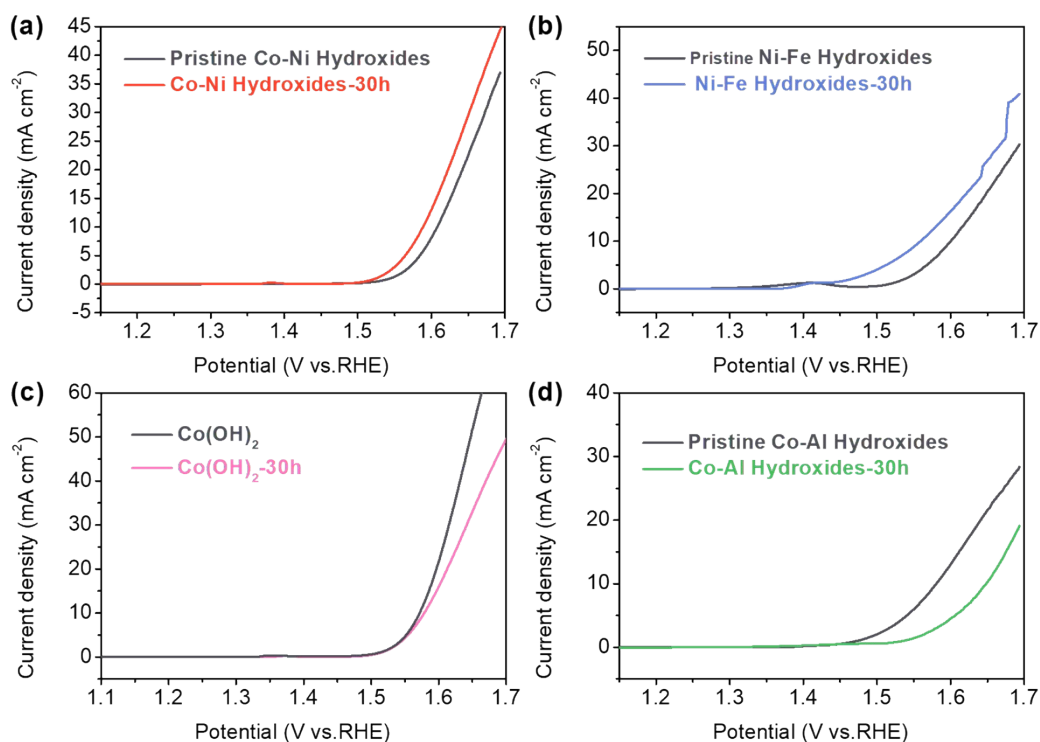


Fig. S12 (a) OER performance of the pristine Co-Ni hydroxides and Co-Ni hydroxides-30h; (b) OER performance of the pristine Ni-Fe hydroxides and Ni-Fe hydroxides-30h. (c) OER performance of the pristine Co(OH)₂ and Co(OH)₂-30h; (d) OER performance of the pristine Co-Al hydroxides and Co-Al hydroxides-30h.

The photo-irradiation method reported here can produce destroyed surface and form defects over layered hydroxide materials, which will influence electrocatalytic performance. However, the produced defects caused by photo-irradiation are not always beneficial to special catalytic activity (e. g. OER). So, the decrease of OER performance over CoAl-hydroxides-30h may be caused that the produced defects and exposed atoms are low active. These results indicate that photo-irradiation method is an effective method to tune the active sites of hydroxide-based materials. However, the change of catalytic performance may not be always positive.

Table 1 Comparisons of OER performance over Ni-based catalysts in alkaline medium.

Catalysts	WE ^{a)}	Electrolyte	J ^{b)}	H ^{c)}	TS ^{d)}	Ref.
α -Ni(OH) ₂ NS	GC	1M KOH	10	351	111	8
β -Ni(OH) ₂ NS-OV	GC	1M KOH	10	369	69	9
NiOOH	GC	1M KOH	10	378	89	10
Ni	GC	1M KOH	10	400	143	11
NiO	GC	1M KOH	10	480	231	12
Ni-Al LDH	GC	1M KOH	10	519	189	11
NiFe LDH	GC	1M KOH	10	330	113	13
B-NiFe LDH	GC	1M KOH	10	229	57	14
Ir-Ni(OH) ₂	GC	1M KOH	10	235	58.4	15
IrO ₂	GC	1M KOH	10	311	54	16
β -Ni(OH) ₂ -30h	GC	1M KOH	10	326	65.6	This work

a) WE is working electrode (GC, Glass carbon); b) J is current density (mA cm⁻²); c)

η is overpotential (mV); d) TS is Tafel slope (mV dec⁻¹).

Table S2 The value of R_s , R_{ct} , and R_{oad} were obtained by fitting the EIS curves

Products	R_s (Ω)	R_{ct} (Ω)	R_{oad} (Ω)
pristine β -Ni(OH) ₂	10.0	10.0	20.1
β -Ni(OH) ₂ -10h	10.2	8.7	34.6
β -Ni(OH) ₂ -20h	10.4	6.3	44.1
β -Ni(OH) ₂ -30h	10.2	5.0	56.7

Table S3 The value of corresponding ΔG_1 , ΔG_2 , ΔG_3 , and ΔG_4 for (100), (011), and (001) facet of β -Ni(OH)₂.

Facet	ΔG_1 (eV)	ΔG_2 (eV)	ΔG_3 (eV)	ΔG_4 (eV)
(001)	0.26	0.57	3.35	0.74
(100)	0.87	0.40	2.32	1.33
(011)	0.62	0.55	1.93	1.82

References

1. T. Kou, S. Wang, J. L. Hauser, M. Chen, S. R. J. Oliver, Y. Ye, J. Guo and Y. Li, *ACS Energy Letters*, 2019, **4**, 622-628.
2. N. Zhang, B. Yang, Y. He, Y. He, X. Liu, M. Liu, G. Song, G. Chen, A. Pan, S. Liang, R. Ma, S. Venkatesh and V. A. L. Roy, *Small*, 2018, **14**, e1803015.
3. Y. Sun, S. Gao, F. Lei and Y. Xie, *Chem Soc Rev*, 2015, **44**, 623-636.
4. A. Y. Faid, A. O. Barnett, F. Seland and S. Sunde, *Electrochimica Acta*, 2020, **361**, 137040.
5. Z. Chen, L. Cai, X. Yang, C. Kronawitter, L. Guo, S. Shen and B. E. Koel, *ACS Catalysis*, 2018, **8**, 1238-1247.
6. S. She, Y. Zhu, H. A. Tahini, X. Wu, D. Guan, Y. Chen, J. Dai, Y. Chen, W. Tang, S. C. Smith, H. Wang, W. Zhou and Z. Shao, *Small*, 2020, **16**, e2006800.
7. J. Huang, Y. Li, Y. Zhang, G. Rao, C. Wu, Y. Hu, X. Wang, R. Lu, Y. Li and J. Xiong, *Angewandte Chemie*, 2019, **131**, 17619-17625.
8. J. Yan, L. Kong, Y. Ji, J. White, Y. Li, J. Zhang, P. An, S. Liu, S. T. Lee and T. Ma, *Nat Commun*, 2019, **10**, 2149.
9. N. Kim, D. Lim, Y. Choi, S. E. Shim and S.-H. Baeck, *Electrochimica Acta*, 2019, **324**, 134868
10. Y. Jin, S. Huang, X. Yue, H. Du and P. K. Shen, *Acs Catalysis*, 2018, **8**, 2359-2363.
11. F. Wang, G. Chen, X. Liu, F. Chen, H. Wan, L. Ni, N. Zhang, R. Ma and G. Qiu, *ACS Sustainable Chemistry & Engineering*, 2018, **7**, 341-349.
12. C. Liao, B. Yang, N. Zhang, M. Liu, G. Chen, X. Jiang, G. Chen, J. Yang, X. Liu, T. S. Chan, Y. J. Lu, R. Ma and W. Zhou, *Advanced Functional Materials*, 2019, **29**, 1904020.
13. C. Peng, N. Ran, G. Wan, W. Zhao, Z. Kuang, Z. Lu, C. Sun, J. Liu, L. Wang and H. Chen, *ChemSusChem*, 2020, **13**, 811-818.
14. I.-K. Ahn, S.-Y. Lee, H. G. Kim, G.-B. Lee, J.-H. Lee, M. Kim and Y.-C. Joo, *RSC Advances*, 2021, **11**, 8198-8206.
15. Y. Xing, J. Ku, W. Fu, L. Wang and H. Chen, *Chemical Engineering Journal*, 2020, **395**, 125149
16. J. Liu, J. Xiao, Z. Wang, H. Yuan, Z. Lu, B. Luo, E. Tian and G. I. N. Waterhouse, *ACS Catalysis*, 2021, **11**, 5386-5395.